Journal of Materials Chemistry C

ROYAL SOCIETY OF CHEMISTRY

PAPER

View Article Online
View Journal | View Issue

Cite this: J. Mater. Chem. C, 2024, 12, 7707

Vacuum-assisted colossal enhancement of up-conversion luminescence of lanthanide-doped nanoparticles upon NIR laser irradiation – a new strategy for phosphor development†

Christian Hernández-Álvarez, *[a] Kevin Soler-Carracedo,[b] Przemysław Woźny, [b] Inocencio R. Martín*[a] and Marcin Runowski *[b]

Received 30th March 2024,
Accepted 29th April 2024

DOI: 10.1039/d4tc01293c

rsc.li/materials-c

Materials science has experienced significant advances in the development of new techniques to synthesize materials with unique properties, which are essential for various applications. For instance, lanthanide-doped structures have been combined with other optically-active compounds to produce materials with unique properties for anti-counterfeiting, bio-applications, optical sensors, photovoltaics, and so on. There are many different chemical synthesis routes (bottom-up; wet chemistry methods) and physical approaches (top-down) to obtain materials, and each of them has its own advantages and disadvantages, depending on the specific requirements of the given material and its final application. This study opens up completely new routes for the precise and localized crystal growth of optical materials and huge enhancement of their up-conversion luminescence intensity (by 2-orders of magnitude). It was possible by irradiation of the initially prepared nanoparticles with the NIR (975 nm) laser under lowered pressure conditions, *i.e.*, vacuum. As exemplary compounds, we used the lanthanide-doped YVO_4 nanomaterials, containing either Yb^{3+}–Tm^{3+} or Yb^{3+}–Er^{3+} ions. It was shown that the loss of air (vacuum) significantly improves the heating rate of the samples and induces the growth of the crystals. In addition, confocal Raman spectroscopy was used to verify the evolution of the materials structure before and after laser treatment.

1. Introduction

The emission of a broad spectrum ranging from UV to NIR light, depending on the physical phenomenon occurring, up-conversion (UC) or down-shifting (DS), has placed luminescent materials doped with rare earth ions in a strategic position for industrial development,[1–8] as they can be used in various fields, such as anti-counterfeiting, solid state lighting, contactless sensing, solar cells, catalysis, nanophotonics, *etc.*[9–16] Given the need for the design of new materials for application in fields such as the manufacture of rare earths, the development of new techniques for the synthesis of materials with unique properties has developed extensively in recent years.[17–20]

There are several techniques available for synthesizing materials, including wet chemistry methods, such as *e.g.* sol–gel, high-temperature calcination, in emulsions, hydrothermal synthesis, and co-precipitation.[3,21–27] On the other hand, there are also physical approaches such as mechanosynthesis in a ball mill, (nano)lithography, laser-ablations, high-temperature evaporation, and so forth.[3,24,25,28,29] Each of these techniques has benefits and drawbacks, and ultimately the choice of the most suitable technique depends on the specific requirements of the material being produced.[24,25,30,31] For example, the sol–gel technique is a versatile method for producing nanomaterials with high crystallinity, high surface-to-volume ratio and controlled porosity. This technique involves the use of solution-state precursors to create solid materials like metal oxides. While the sol–gel technique offers many advantages, it may be limited by factors such as cost and scalability.[21–25] In contrast, hydrothermal synthesis involves using high temperatures and pressures to synthesize materials in an aqueous solution. This technique offers the advantage of producing materials with high crystallinity and controlled morphology, but it can be limited by the requirement for specialized equipment to achieve the necessary conditions of high temperatures and pressure. Moreover, this technique is quite energy- and time-consuming.[25–27] Similar, to the sol–gel technique, evaporation under vacuum synthesis is another straightforward technique that involves evaporating a material and then

[a] Universidad de La Laguna, Departamento de Física, MALTA- Consolider Team, IMN and IUdEA Apdo. Correos 456, E-38206, San Cristóbal de La Laguna, Santa Cruz de Tenerife, Spain. E-mail: chernaal@ull.edu.es, imartin@ull.edu.es
[b] Adam Mickiewicz University, Faculty of Chemistry, Uniwersytetu Poznańskiego 8, 61-614 Poznań, Poland. E-mail: runowski@amu.edu.pl

† Electronic supplementary information (ESI) available. See DOI: https://doi.org/10.1039/d4tc01293c

condensing it to form a solid. This technique is suitable for producing materials with high purity but can be limited by the need for high vacuum conditions (10^{-3}–10^{-7} mbar), which can be challenging and expensive to achieve as in the hydrothermal technique.[24,25]

Among current techniques that utilize lasers to either remove or synthesize a desired material, the following approaches are most common: laser ablation, pulse laser deposition (PLD), and selective laser melting (SLM).[25,32] Typically, laser ablation refers to the removal of surface material using a pulse of laser radiation, but it is also possible to achieve material ablation with a continuous flow of laser radiation if the beam energy is high enough.[33–35] On the other hand, PLD is capable of reproducing almost any type of material (oxides, metals, polymers). Its high stoichiometric, reproducibility and versatility make it one of the most powerful techniques for producing complex oxides, magnetoelectric multiferric materials, and diluted magnetic semiconductors, among others.[36,37] In contrast, the SLM technique is a process in which a laser beam is used to melt and fuse together layers of powdered material, typically metal, to create a solid object. This process is commonly used in additive manufacturing, also known as 3D printing.[38,39]

In addition, with the current interest in lanthanide-doped materials, new laser treatment techniques are being developed to modify the materials. For example, Dangli *et al.*[40,41] show in some of their papers how single $NaYbF_4$:Ho^{3+}@YbOF:Ho^{3+} heterojunctions with unique morphologies including hollow spheres, lollipops and sponge-like plates can be successfully prepared by deliberately controlling the precursor particles and light welding parameters, where the oxidation reaction with $NaYbF_4$:Ho^{3+} microcrystals was induced by increasing the excitation power density and irradiation duration, which resulted in a $NaYbF_4$ and YbOF heterojunction with lattice mismatch, thus improving their luminescent properties.

In this work, we show for the first time the use of a NIR laser in combination with a vacuum for remelting of nanoparticles and the growth of larger crystals of lanthanide-based, energy up-converting materials in a micron-sized, well-localized area (as schematically shown in Fig. 1a). Thanks to the improved light-to-heat conversion under vacuum, the optical heating of the nanoparticles can occur at moderate laser power ($\approx$3 kW cm^{-2}), and the UC emission intensity of the irradiated structures was permanently boosted by 2-orders of magnitude. Fig. 1b shows the radiative and non-radiative processes occurring in the systems

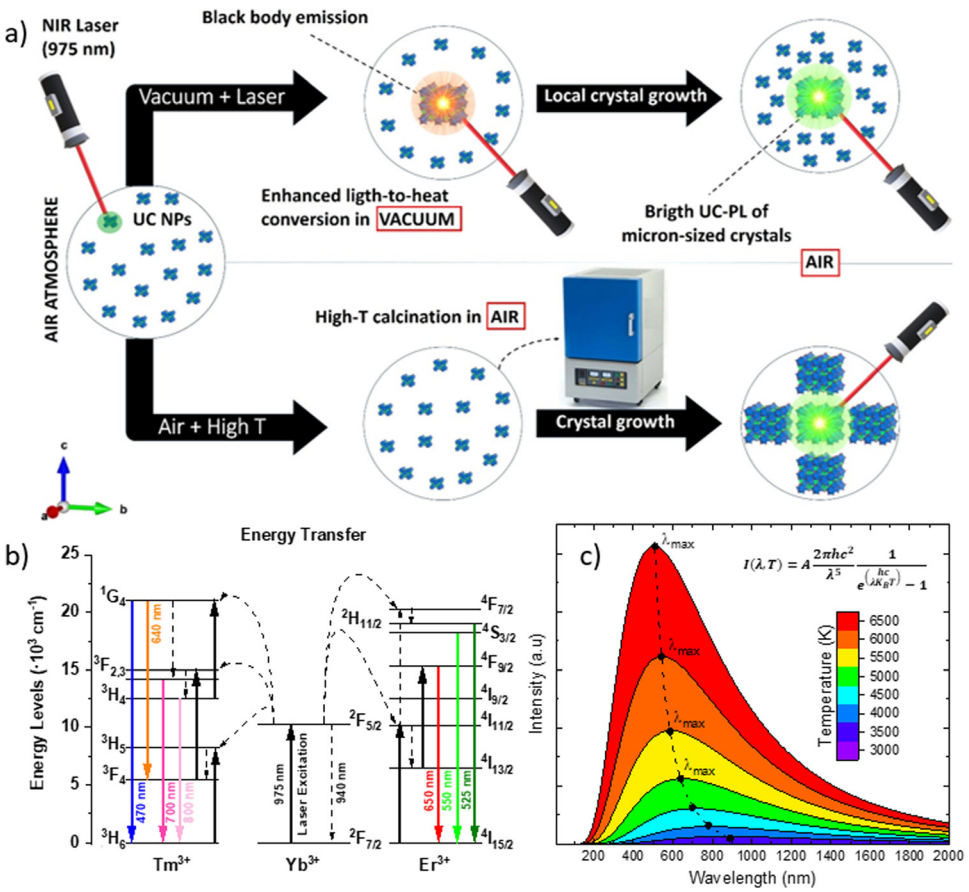

Fig. 1 (a) Scheme of crystal growth procedures applied to the samples, including laser-induced and vacuum enhanced optical heating and remelting, and a conventional high-temperature calcination. (b) Simplified energy-level diagram for Yb^{3+}–Tm^{3+} and Yb^{3+}–Er^{3+} in the studied systems. (c) Spectral intensity distribution of Planck's black-body radiation as a function of wavelength for different temperature values (the maximum of the intensity shifts to shorter wavelength as the black-body temperature increases).

studied, *i.e.*, yttrium vanadate (YVO_4) nanoparticles doped with Yb^{3+}–Tm^{3+} and Yb^{3+}–Er^{3+} ions. Given the novelty of this technique, vanadate was selected as a matrix due to its high melting point (~1800 °C),[42] as the material is expected to undergo high temperatures during the vacuum process. Other materials (like simple or complex oxides, garnets, apatites, silicates, phosphates, borates, *etc.*) should also work with this method. It is important, however, to avoid materials with relatively low phase transition temperature, such as fluorides whose phase transition is around 500 °C. In addition, an analysis of the generated black body emission was performed and correlated with the expected temperature values (based on the Planck's law) to know the average, local temperature reached by the sample within the laser spot under vacuum. This can be seen in Fig. 1c, showing the relationship between the temperature and the spectral distribution of the black body radiation. Moreover, we performed a comprehensive Raman analysis to investigate the structural features of the materials before and after laser treatment, compared to the materials annealed under high-temperature conditions.

2. Results and discussion

2.1 Structural study

Fig. 2a shows the arrangement of the atoms in the tetragonal YVO_4 from $I4_1/amd$ space group (JCPDS no. 82-1968), *i.e.*, in the compounds that have been synthesized and doped with the corresponding lanthanide ions. Fig. 2b shows the powder X-ray diffraction (PXRD) patterns of the sample synthesized under hydrothermal conditions (low-*T* synthesis) and the calcined one, *i.e.*, post-treated under high-temperature conditions (high-*T* synthesis), both corresponding to the tetragonal YVO_4

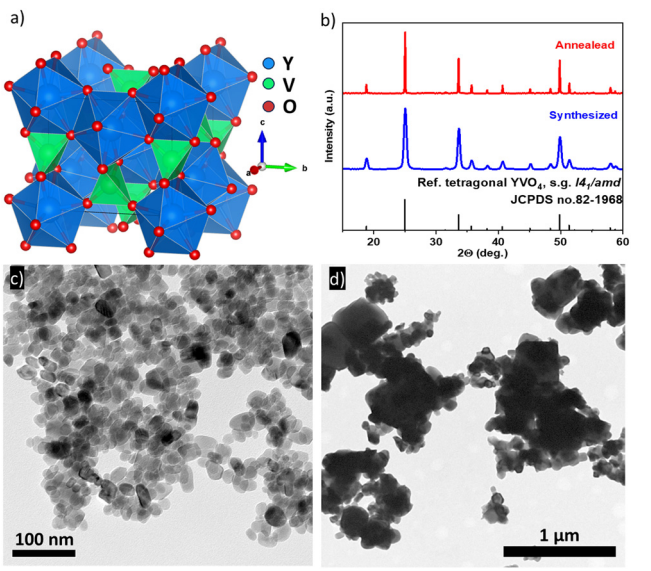

Fig. 2 (a) 3D representation of the tetragonal YVO_4 ($I4_1/amd$) structure. (b) Comparison of the PXRD patterns with the reference data. (c) and (d) Representative TEM images of the hydrothermally synthesized nanomaterial (c) with the sample annealed at high-temperature (d).

mentioned above. It is clear that the reflexes of the annealed sample are much narrower, which is simply due to the larger crystal sizes and their better crystallinity, compared to the product obtained under hydrothermal conditions. Additionally, the transmission electron microscopy (TEM) images shown in Fig. 2c and d confirm much smaller size (≈10–20 nm) of the crystals formed at low-temperature conditions in solution (c), in contrast to the larger crystals (≈300–500 nm) of the calcined sample (d). In the following sections, we discuss in detail how the treatment of the nano-sized samples treated with a laser (in vacuum) can favor the growth of crystals, thus improving the efficiency of their luminescence.

2.2 Laser treatment under vacuum

Fig. 3a shows the UC emission spectra of the hydrothermally synthesized YVO_4:20%Yb^{3+},0.5%Tm^{3+} sample (nanoparticles) under 975 nm laser excitation, measured at variable pressure and a fixed laser power (≈3.3 kW cm^{-2}). Initially, at ambient pressure, no emission signal from the Yb^{3+}–Tm^{3+} ions was detected, and this could be due to the very low UC emission efficiency of Tm^{3+} in the studied nanoparticles, caused by the relatively low synthesis temperature (150 °C), and therefore lower crystallinity level and smaller crystal sizes, compared to other reports, where the Tm^{3+} samples were annealed and do show UC emission without post-treatment.[43–45] Then, as the vacuum increases, the blackbody emission starts to be observed, due to the laser-induced optical heating of the material, which is significantly boosted under vacuum. This effect is a result of enhanced light-to-heat conversion at lowered pressure. Finally, when the sample returns to ambient pressure (so it is cooled down), the blue emission of the Yb^{3+}–Tm^{3+} system can be observed. However, at this stage, the sample is still "hot", due to the high laser power density used, and the band associated with thermalization processes in Tm^{3+} (at 700 nm) can be observed. When the pump power density is reduced, the characteristic blue emission peak of Tm^{3+}, located at 470 nm, gradually appeared (see Fig. 3b), and the total emission intensity increases, as the laser-induced thermal quenching became much less pronounced.

A similar experiment was conducted using YVO_4:20%-Yb^{3+},2%Er^{3+} nanoparticles, which were synthesized at low-temperature conditions, as well. In this second experiment, we wanted to confirm the possibility of improving the luminescence of the sample by applying a laser treatment in a vacuum environment. In Fig. 3c, the corresponding UC emission spectra under 975 nm laser excitation, recorded at variable pressure conditions and fixed pump power of 3.3 kW cm^{-2}, are presented. It is clearly seen that at the beginning (at ambient pressure), the emission bands of Er^{3+} ions located around 525 ($^2H_{11/2} \rightarrow {}^4I_{15/2}$) and 550 nm ($^4S_{3/2} \rightarrow {}^4I_{15/2}$) transitions have very low intensity. However, in contrast to Tm^{3+} ions, in this case we could detect some signal and pale green emission of Er^{3+} even at this stage of the experiment was observed, which is due to much better UC efficiency in the Yb^{3+}–Er^{3+} system. When the vacuum was turned on, the black body emission appeared in the low-energy part of the spectra, and the Er^{3+} ion

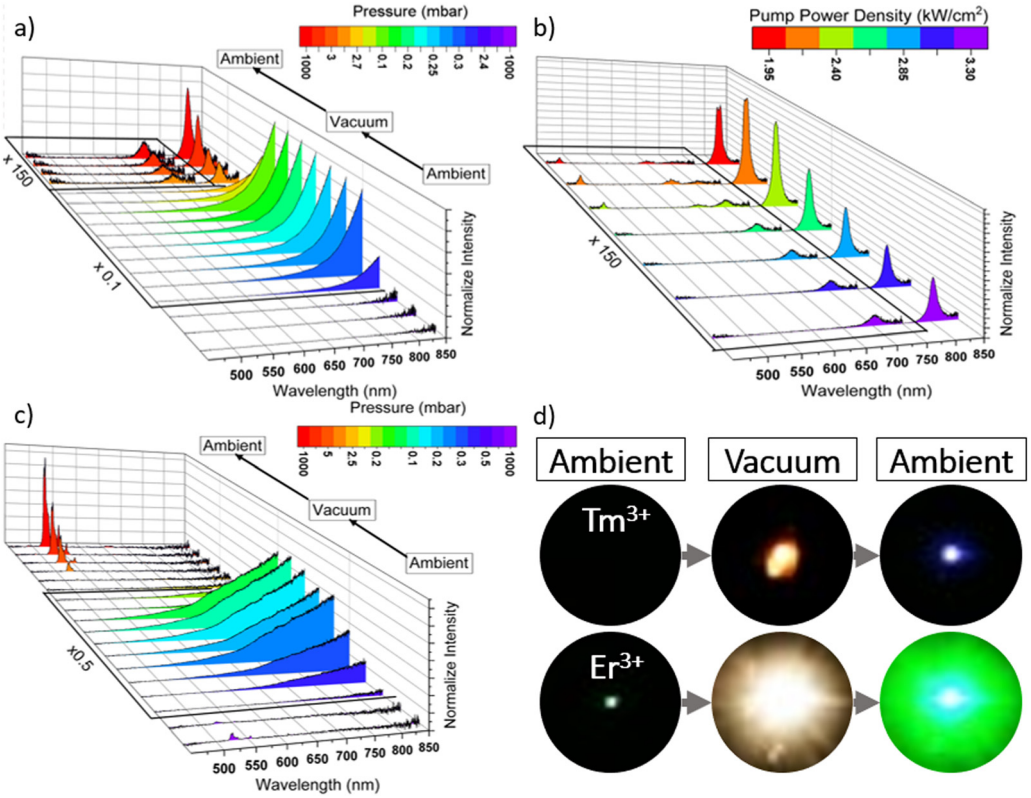

Fig. 3 (a) UC emission spectra of the hydrothermally synthesized sample YVO_4:20%Yb^{3+},0.5%Tm^{3+} recorded in the cycle at different pressure values upon NIR 975 nm laser irradiation (excitation flux ≈3.3 kW cm^{-2}), and (b) the corresponding spectra as a function of pump power density. (c) UC emission spectra of the hydrothermally synthesized YVO_4:20%Yb^{3+},2%Er^{3+} sample recorded in the cycle at different pressure values upon NIR 975 nm laser irradiation (excitation flux ≈3.3 kW cm^{-2}). (d) Photographs of UC luminescence for both samples irradiated with NIR light, taken at different steps of laser treatment, *i.e.*, at ambient conditions and under vacuum.

emission disappeared, due to the huge increase of the local temperature, leading to the significant thermal quenching of the UC emission. Importantly, after turning the vacuum off, and reaching the atmospheric pressure value, the bright green UC luminescence of Er^{3+} permanently appears, and its intensity is significantly enhanced compared to the initial signal. Note, that the band intensity ratio of Er^{3+} ions (525/550 nm) indicated the high local temperature of the irradiated sample. Fig. S1 (ESI†) shows the corresponding UC emission spectra of this material recorded with the same system (after the experiment), by measuring the spectra at decreasing laser power. It is clear, that the emission intensity of the Er^{3+} ions increased even more (due to the limited thermal quenching) and the 525/550 nm band ratio decreased, as the sample cooled down to room temperature, and the laser heating was not further observed. The different steps of both experiments can also be visually seen in Fig. 3d, which depicts digital photographs of both samples upon NIR laser irradiation, taken at ambient pressure and under vacuum. In the first case of the YVO_4:Yb^{3+}–Tm^{3+}, it is not possible to observe any luminescence until the sample has been exposed to vacuum conditions and returned to ambient pressure. Only then, the typical blue emission of Tm^{3+} is observed. Whereas, in the case of the YVO_4:Yb^{3+}–Er^{3+} sample, a huge enhancement of green up-conversion emission of Er^{3+} ions after laser exposure under vacuum can be observed. Note that in both cases, under vacuum conditions and simultaneous laser irradiation, ultra-bright black body emission can be observed, and for the Er^{3+}-doped sample it is even brighter (most probably due to better light-to-heat conversion efficiency for this material). In fact, using the Plank equation and the spectral distribution of the generated thermal emission, we estimated the local temperature elevation for the materials irradiated under vacuum at 1422 K and 1769 K for the Tm^{3+} and Er^{3+} doped samples, respectively (see details in the ESI† file). The obtained results agree well with our previous findings, confirming stronger optical heating effect and higher local temperature for the Er^{3+}-doped sample, achieved upon its laser treatment under vacuum.

Fig. 4a shows a photograph of a region of the YVO_4:Yb^{3+}–Tm^{3+} sample that has received laser treatment (within the incident laser beam spot), and that can be easily distinguished as having a different appearance from the nearby areas. It can clearly be seen that only in the irradiated area, where the material was subjected to the laser treatment (leading to the huge elevation of the local temperature of the sample), the sample material was molten leading to recrystallization of the grains and crystal growth. This area was analyzed under a confocal microscope, by mapping a series of emission spectra recorded under laser excitation. Fig. 4b shows the results of this mapping, representing the collected integrated emission

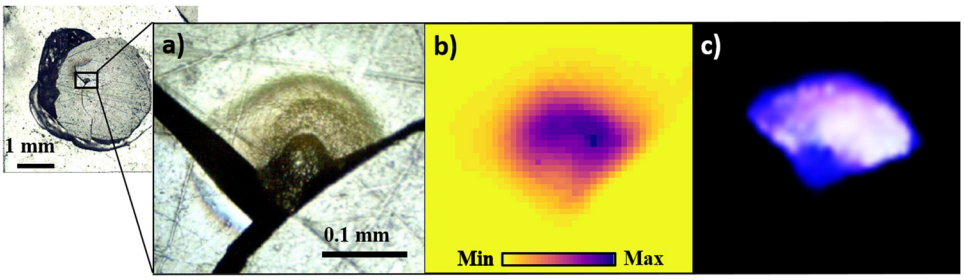

Fig. 4 (a) Photograph of the sample YVO_4:Yb^{3+}–Tm^{3+} taken at ambient conditions (after the laser post-treatment under vacuum), with a zoomed-in view of the irradiated zone under normal light. (b) Mapping of the corresponding sample luminescence signal under a confocal microscope, representing the integrated emission from materials, where the maximum signal intensity is denoted as dark purple. (c) Photograph of the sample zone irradiated with a NIR (975 nm) laser taken at ambient conditions, showing its bright blue UC emission achieved after laser treatment under vacuum.

intensity, *i.e.*, luminescence signal from the sample. The purple color denotes the maximum intensity of the signal, which is located in the central part of the material corresponding to the previously irradiated area (during the experiment performed under vacuum conditions), and the untreated area of the Tm^{3+}-doped sample (nanoparticles synthesized at low-*T*) did not reveal any luminescence. Fig. 4c presents a digital photograph of the analyzed area upon NIR 975 nm laser irradiation (ambient conditions), clearly showing its bright blue emission, due to UC emission of the Yb^{3+}–Tm^{3+} system (corresponding well to the photograph in Fig. 3d).

2.3 Raman spectroscopy

In this section, a comparison of the Raman spectra is made to verify that there is no phase transition in the hydrothermally synthesized materials before and after laser treatment under vacuum and after standard annealing in a furnace, to check if they have the same tetragonal structure of YVO_4. Fig. 5 shows three Raman spectra, the one in red is the spectrum of the hydrothermally synthesized sample at low temperature (before the vacuum and laser treatment), the black one corresponds to the material where the laser treatment under vacuum conditions was applied, and the blue one comes from the sample annealed in a furnace at high temperature. As it can be observed, there is an evident increase of the crystallinity level (more intense Raman signal) for the annealed and laser treated samples, compared to the untreated material obtained during the hydrothermal synthesis. The obtained results agree well with luminescence data, showing that the calcined or laser-treated (in vacuum) samples have much higher crystallinity level (and larger crystals), which is associated with their significantly improved UC luminescence intensity. Moreover, in all cases the recorded Raman spectra have the same shape, and they coincide well as there are no additional peaks observed (see Fig. 5), confirming that all materials have the same structure of the tetragonal phase of YVO_4.[46–50]

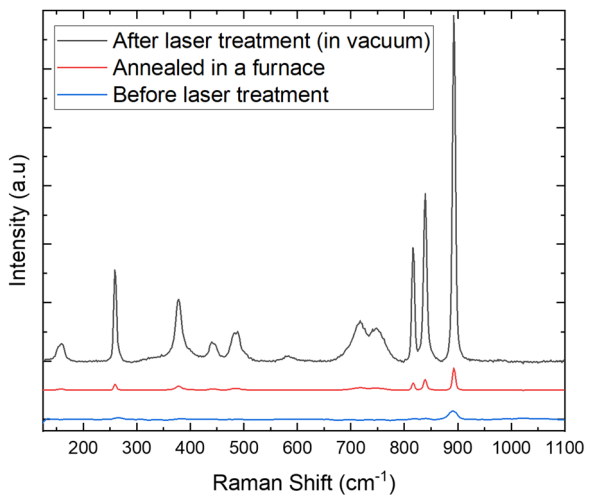

Fig. 5 Raman spectra of the hydrothermally synthesized YVO_4:Yb^{3+}–Tm^{3+}, before and after laser treatment under vacuum and after standard annealing in a furnace.

2.4 Luminescence comparison of the annealed and laser-treated samples

Fig. 6a and b show the emission spectra at fixed power densities of 0.9 kW cm^{-2}, for the Er^{3+}-doped (a) and Tm^{3+}-doped (b) samples, which were either annealed in a furnace or treated with a laser (in vacuum) after hydrothermal synthesis. The laser treatment under vacuum results in even better UC emission intensity, compared to the annealed samples, demonstrating that the type of the applied post-synthesis treatment method also has a significant impact on the luminescence efficiency of the sample. This is plausibly because the temperature values reached for the laser treatment under vacuum were higher (*ca.* 1420–1770 K), compared to the ones achieved during the standard annealing process ($\approx$1273 K), leading to better crystallinity and larger crystal sizes of the final products.

2.5 Crystal size

Fig. 7a shows the pellet made of the nanoparticles from the hydrothermal synthesis. We highlight two regions: in red (Fig. 7b) where the laser treatment is performed with a vacuum and clearly shows a crater, where the crystals are larger than those found in the blue region (Fig. 7c), which is unaltered and shows a homogeneous surface with tiny dots that are the small particles of the material. In addition, an interesting effect can be observed in Fig. 7d, *i.e.* the crystals are smaller moving away from the area where the laser hits the material, since the generated heat (*via* vacuum-enhanced light-to-heat conversion)

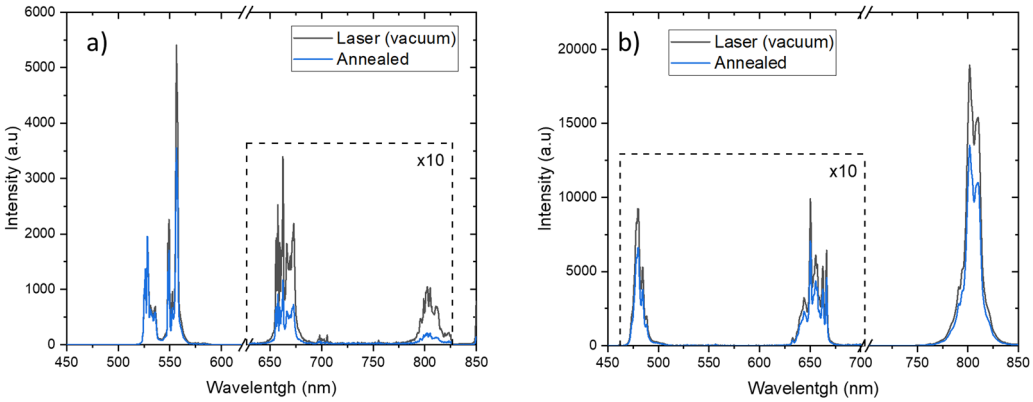

Fig. 6 (a) Differences in UC intensities between the two samples: YVO_4:20%Yb^{3+},2%Er^{3+} annealed and after the laser treatment under vacuum at 0.9 kW cm^{-2}. (b) Differences in the UC intensities between the two samples: YVO_4:20%Yb^{3+},0.5%Tm^{3+} annealed and after the laser treatment under vacuum at 1.5 kW cm^{-2}.

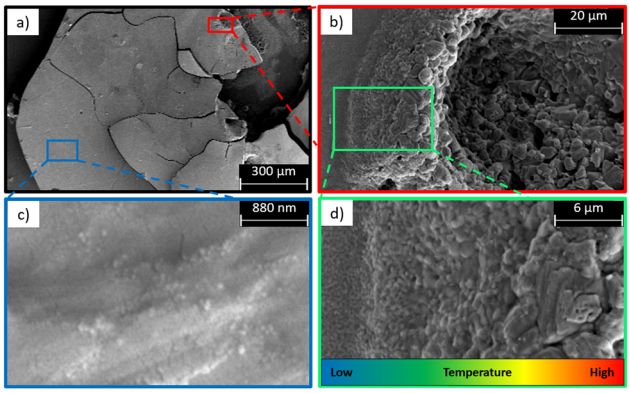

Fig. 7 Representative SEM images of the YVO_4:20%Yb^{3+},2%Er^{3+} pellet (a), showing the laser-treated (b), untreated (c) and surroundings of the laser-treated (d) regions.

is dissipated by conduction, transmitting the heat to the nearby particles.

Considering alternative approaches for the material synthesis, one could calcinate luminescent materials in a furnace either in a gas atmosphere (*e.g.*, O_2, N_2, H_2, *etc.*) or under vacuum conditions. However, in the case of the vanadate materials studied, the constituting lanthanide ions do not undergo red-ox reactions in the presence of oxygen or a reducing atmosphere, and hence we do not expect any significant differences in the case of the potential calcination process under vacuum conditions (in the furnace) *vs.* air atmosphere. The postulated effect, *i.e.*, the impact of calcination atmosphere, could have some non-negligible effects in the case of *e.g.*, semiconductive nanoparticles (such as quantum dots), or other gas-sensitive materials where the possible surface defects induced by gas molecules might affect the surface characteristics of the investigated materials. Those effects are important especially in the case of very small nanocrystals (with high surface-to-volume ratio and high surface energy), which remain relatively small after the calcination process. Whereas in our case the particles after the calcination process are relatively large (≈300–500 nm), and the mentioned surface-related effects and the calcination atmosphere should not have a significant effect on the final, spectroscopic properties of the calcinated vanadate materials. Moreover, because of the high thermal stability of the YVO_4 materials, no changes in the composition of the material surface are expected.

3. Conclusion

In this work, we have demonstrated for the first time, a new technique for permanent enhancement of the UC luminescence, by laser-induced crystal growth under vacuum conditions. This technique has been successfully applied to the YVO_4:Yb^{3+}–Tm^{3+} and YVO_4:Yb^{3+}–Er^{3+} nanoparticles. The results showed that the loss of air in the vacuum chamber favored optical heating of the samples and melting and recrystallization of the studied materials, leading to enhanced UC emission in the samples treated with a NIR laser under vacuum. The temperature of the sample during treatment was determined by analyzing the generated blackbody radiation, allowing a comparison with the corresponding temperature values applied during the other synthesis methods (materials annealing in a furnace). Moreover, Raman spectroscopy was used to confirm that there were no phase transitions in the samples, indicating that the crystallinity level was significantly improved during the optical heating under vacuum conditions. Overall, this study demonstrates the potential of using optical heating with laser and vacuum techniques for growing materials with unique and enhanced spectroscopic properties, especially for improving their optical activity, *i.e.*, UC luminescence intensity.

4. Experimental section

4.1 Materials

The starting lanthanide oxide materials, *i.e.*, Y_2O_3, Yb_2O_3, Er_2O_3 and Tm_2O_3 (99.99%) were purchased from Alfa Aesar. Lanthanide oxides were dissolved in an excess of HCl (ASC, 37%) purchased from Sigma-Aldrich and deionized water. Prepared

solutions were evaporated 3-times to dispose of chloric acid. The YCl_3, $YbCl_3$, $ErCl_3$ and $TmCl_3$ salts were diluted with deionized water to prepare 0.5 M solutions. The NH_4VO_3 (ASC, ≥99%) and the cetyltrimethylammonium bromide (CTAB) (≥98%) were purchased from Sigma-Aldrich. The sodium hydroxide (pure p.a., 98.8%) and the trisodium citrate dihydrate (ASC, ≥99%) were purchased from POCH. The NaOH was dissolved in deionized water and diluted to a 1.5 M solution for further pH adjustment.

4.2 Synthesis

Stoichiometric amounts of the appropriate YCl_3, $YbCl_3$, $ErCl_3$ and $TmCl_3$ salt solutions for 1 mmol of YVO_4:20%Yb^{3+},0.5%Tm^{3+} and YVO_4:20%Yb^{3+},2%Er^{3+} were mixed in 15 ml of deionized water with 0.4175 g of trisodium citrate dihydrate and 0.4957 g of CTAB as a surface active agent, respectively. Next, NH_4VO_3 was dissolved in 20 ml of deionized water on heating to obtain a transparent yellow solution. NH_4VO_3 solutions were added dropwise at room temperature to chloride salt and surfactant solutions upon stirring. Finally, the pH was adjusted to 10 using a 1.5 M solution of NaOH upon stirring. The obtained yellow opaque (CTAB) or transparent (sodium citrate) mixture was transferred to a Teflon-lined vessel and was hydrothermally treated for 20 h at 150 °C. As synthesized nanoparticles were centrifuged from the solution and washed with deionized water three times. The obtained materials were dried at 80 °C for 24 h and ground in an agate mortar. The materials were annealed at 1000 °C for 2 h to decompose organic residues, improve the crystallinity level, increase the crystal sizes and enhance their luminescence intensity.

4.3 Characterization

For all experiments, a pellet (≈270 μm thick) was made from the material and placing the material on a small glass plate. UC emission spectra were recorded in the visible range using an Ocean Optics HR4000 High-Resolution Fiber Optic Spectrometer. The excitation source was a tunable continuous-wave (CW) Ti:Sapphire laser system, Spectra Physics 3900S pumped with a 15 W, 532 nm Spectra Physics Millenia, adjusted at 975 nm. In order to measure the laser power, a photodiode (Ophir StarLite) was used. Also, for low pressure measurements, a vacuum was obtained using an oil pump (Edwards RV3), connected to a vacuum chamber, where the manometer was connected to a digital controller (Edwards Active Gauge Controller Single Display). Finally, Raman measurements were obtained using a confocal Raman microscope (Renishaw InVia) with a laser of λ = 785 nm.

Conflicts of interest

There are no conflicts to declare.

Acknowledgements

This work was financially supported by Ministerio de Ciencia e Innovacion of Spain (MICIIN) under the National Program of Sciences and Technological Materials (PID2019-106383GB-C44 and PID2019-107335RA-I00) and Gobierno de Canarias (PROID2021010102 and PROID2020010067) and EU-FEDER funds. This work was supported by the Polish National Science Centre, grant no. 2023/50/E/ST5/00021.

References

1 T. Zheng, M. Runowski, P. Woźny, S. Lis and V. Lavín, *J. Mater. Chem. C*, 2020, **8**, 4810–4817.
2 Y. Hua and J. S. Yu, *ACS Sustainable Chem. Eng.*, 2021, **9**, 5105–5115.
3 X. Qin, X. Liu, W. Huang, M. Bettinelli and X. Liu, *Chem. Rev.*, 2017, **117**, 4488–4527.
4 W. Zheng, P. Huang, D. Tu, E. Ma, H. Zhu and X. Chen, *Chem. Soc. Rev.*, 2015, **44**, 1379–1415.
5 T. Zheng, M. Runowski, J. Xue, L. Luo, U. R. Rodríguez-Mendoza, V. Lavín, I. R. Martín, P. Rodríguez-Hernández, A. Muñoz and P. Du, *Adv. Funct. Mater.*, 2023, **33**, 2214663.
6 M. Runowski, P. Woźny, S. Lis, V. Lavín and I. R. Martín, *Adv. Mater. Technol.*, 2020, **5**, 1901091.
7 K. Soler-Carracedo, I. R. Martin, M. Runowski, L. L. Martín, F. Lahoz, A. D. Lozano-Gorrín and F. Paz-Buclatin, *Adv. Opt. Mater.*, 2020, **8**, 2000678.
8 M. Runowski, P. A. Wony and I. R. Martín, *J. Mater. Chem. C*, 2021, **9**, 4643–4651.
9 M. Runowski, S. Goderski, D. Przybylska, T. Grzyb, S. Lis and I. R. Martín, *ACS Appl. Nano Mater.*, 2020, **3**, 6406–6415.
10 Y. Liu, D. Tu, H. Zhu and X. Chen, *Chem. Soc. Rev.*, 2013, **42**, 6924–6958.
11 C. Hernández-Álvarez, G. Brito-Santos, I. R. Martín, J. Sanchiz, K. Saidi, K. Soler-Carracedo, U. Marciniak and M. Runowski, *J. Mater. Chem. C*, 2023, **11**, 1221–1229.
12 C. Chen, C. Li and Z. Shi, *Adv. Sci.*, 2016, **3**, 1600029.
13 A. Tymiński, E. Śmiechowicz, I. R. Martín and T. Grzyb, *ACS Appl. Nano Mater.*, 2020, **3**, 6541–6551.
14 G. Brito-Santos, B. Gil-Hernández, I. R. Martín, R. Guerrero-Lemus and J. Sanchiz, *RSC Adv.*, 2020, **10**, 27815–27823.
15 G. Brito-Santos, C. Hernández-Rodríguez, B. Gil-Hernández, B. González-Díaz, I. R. Martín, R. Guerrero-Lemus and J. Sanchiz, *Dalton Trans.*, 2022, **51**, 3146–3158.
16 X. Chen, D. Peng, Q. Ju and F. Wang, *Chem. Soc. Rev.*, 2015, **44**, 1318–1330.
17 X. Chen, D. Peng, Q. Ju and F. Wang, *Chem. Soc. Rev.*, 2015, **44**, 1318–1330.
18 R. Zaiter, M. Dussauze, M. Nalin, E. Fargin, F. Adamietz, S. Danto, O. Toulemonde and T. Cardinal, *J. Alloys Compd.*, 2022, **912**, 165181.
19 S. González-Pérez, J. Sanchiz, B. González-Díaz, S. Holinski, D. Borchert, C. Hernández-Rodríguez and R. Guerrero-Lemus, *Surf. Coat. Technol.*, 2015, **271**, 106–111.
20 F. Zhang, Y. Wan, T. Yu, F. Zhang, Y. Shi, S. Xie, Y. Li, L. Xu, B. Tu and D. Zhao, *Angew. Chem., Int. Ed.*, 2007, **46**, 7976–7979.
21 A. C. Pierre, *Introduction to Sol–Gel Processing*, Springer International Publishing AG, Cham, 2020.

22 J. D. Mackenzie, *J. Non Cryst. Solids*, 1988, **100**, 162–168.
23 M. A. Aegerter and M. Mennig, *Sol-Gel Technologies for Glass Producers and Users*, Springer Science & Business Media, 2013.
24 N. Abid, A. M. Khan, S. Shujait, K. Chaudhary, M. Ikram, M. Imran, J. Haider, M. Khan, Q. Khan and M. Maqbool, *Adv. Colloid Interface Sci.*, 2022, **300**, 102597.
25 A. M. El-Khawaga, A. Zidan and A. I. A. A. El-Mageed, *J. Mol. Struct.*, 2023, **1281**, 135148.
26 A. Szczeszak, T. Grzyb, Z. Śniadecki, N. Andrzejewska, S. Lis, M. Matczak, G. Nowaczyk, S. Jurga and B. Idzikowski, *Inorg. Chem.*, 2014, **53**, 12243–12252.
27 M. Runowski and S. Lis, *J. Alloys Compd.*, 2016, **661**, 182–189.
28 D. Sugak, L. Vasylechko, V. Sydorchuk, S. Hurskyy, A. Luchechko, I. I. Syvorotka, A. Lakhnik, U. Yakhnevych, V. Hreb and S. Ubizskii, *Powders*, 2023, **2**, 562–577.
29 M. Fabián, B. I. Arias-Serrano, J. Briančin and A. Yaremchenko, *J. Alloys Compd.*, 2023, **965**, 171374.
30 G. Dhanaraj, K. Byrappa, M. Dudley and V. Prasad, Crystal Growth Techniques and Characterization: An Overview, *Springer Handbook of Crystal Growth*, Springer-Verlag, Berlin, Heidelberg, 2010.
31 H. J. Scheel, *The Development of Crystal Growth Technology, The Development of Crystal Growth Technology*, John Wiley & Sons, Ltd, Chichester, UK, 2003, p. 1.
32 D. Zhang, B. Gökce and S. Barcikowski, *Chem. Rev.*, 2017, **117**, 3990–4103.
33 R. E. Russo, X. Mao, H. Liu, J. Gonzalez and S. S. Mao, *Talanta*, 2002, **57**, 425–451.
34 C. R. Phipps, *Laser Ablation and its Applications*, Springer, New York, NY, 2006.
35 R. E. Russo, X. L. Mao, J. Yoo and J. J. Gonzalez, in *Chapter 3 - Laser Ablation*, ed. J. P. Singh and S. N. Thakur, Elsevier, Amsterdam, 2007, p. 41.
36 R. Eason, *Pulsed Laser Deposition of Thin Films: Applications-Led Growth of Functional Materials*, John Wiley & Sons, 2007.
37 J. Schou, *Appl. Surf. Sci.*, 2009, **255**, 5191–5198.
38 J. P. Kruth, L. Froyen, J. Van Vaerenbergh, P. Mercelis, M. Rombouts and B. Lauwers, *J. Mater. Process. Technol.*, 2004, **149**, 616–622.
39 C. Y. Yap, C. K. Chua, Z. L. Dong, Z. H. Liu, D. Q. Zhang, L. E. Loh and S. L. Sing, *Appl. Phys. Rev.*, 2015, 2.
40 D. Gao, P. Wang, J. Wu, J. Gao, G. Xiao, A. Cai and K. Ma, *Nano Sel.*, 2021, **2**, 398–405.
41 D. Gao, D. Zhao, H. Xin, A. Cai and X. Zhang, *J. Mater. Chem. C*, 2019, **7**, 11879–11886.
42 S. Erdei and F. W. Ainger, *J. Cryst. Growth*, 1993, **128**, 1025–1030.
43 M. Runowski, P. Woźny, N. Stopikowska, I. R. Martín, V. Lavín and S. Lis, *ACS Appl. Mater. Interfaces*, 2020, **12**, 43933–43941.
44 Y. Cheng and K. Sun, *J. Nanopart. Res.*, 2018, **20**, 1–13.
45 J. Miao, Y. Wen, W. Wang, J. Su, J. Xu, P. Zhong and W. Rao, *J. Mater. Sci.: Mater. Electron.*, 2015, **26**, 6178–6181.
46 J. Mitric, U. Ralevic, M. Mitric, J. Airkovic, M. RomAevic, M. Gilic and N. RomAevic, *J. Raman Spectrosc.*, 2019, **50**, 802–808.
47 Y. K. Voron'ko, A. A. Sobol, V. E. Shukshin, A. I. Zagumennyī, Y. D. Zavartsev and S. A. Kutovoī, *Phys. Solid State*, 2009, **51**, 1886–1893.
48 B. Jin, S. Erdei, A. S. Bhalla and F. W. Ainger, *Mater. Lett.*, 1995, **22**, 281–284.
49 Saloni and A. Khanna, *J. Mater. Sci.: Mater. Electron.*, 2023, **34**, 70.
50 I. E. Kolesnikov, E. V. Golyeva, M. A. Kurochkin, E. Y. Kolesnikov and E. Lähderanta, *J. Lumin.*, 2020, **219**, 116946.

